SCIENCE CHINA
Information Sciences

• RESEARCH PAPER •

February 2024, Vol. 67, Iss. 2, 122402:1–122402:12
https://doi.org/10.1007/s11432-022-3698-7

Geometry characteristics and wide temperature behavior of silicon-based GaN surface acoustic wave resonators with ultrahigh quality factor

Guofang YU[1,2], Renrong LIANG[1,2*], Haiming ZHAO[1,2], Lei XIAO[1,2], Jie CUI[1,2], Yue ZHAO[1,2], Wenpu CUI[1,2], Jing WANG[1,2], Jun XU[1,2], Jun FU[1,2*] & Tianling REN[1,2]

[1]*School of Integrated Circuits, Tsinghua University, Beijing* 100084*, China;*
[2]*Beijing National Research Center for Information Science Technology, Tsinghua University, Beijing* 100084*, China*

Received 19 July 2022/Revised 19 October 2022/Accepted 8 February 2023/Published online 30 October 2023

Abstract Surface acoustic wave (SAW) resonators with an ultrahigh Q-factor are designed and fabricated on silicon-based gallium nitride (GaN/Si). The temperature-dependent performance is characterized over a wide range, from 10 to 500 K. Finite element analysis is employed to guide the design of the SAW resonator from indications of the Rayleigh mode and weak propagation direction dependence of SAW in the *c*-plane of GaN/Si. The SAW resonator with 100 pairs of interdigital transducers (IDT), 100 pairs of grating reflectors (GR) for each side, aperture size of 80 µm, metallization ratio of 0.5, and electrode width of 500 nm resonates at 1.9133 GHz accordingly with an ultrahigh Q-factor of 7622 at room temperature, which contributes the $f_r \times Q_r$, up to 14.583×10^{12} Hz. A resonator operating over 10 to 500 K indicates an approximately linear decreasing temperature dependence above 280 K while being approximately constant below 40 K. The fitting to resonator characteristics using the modified Butterworth Van Dyke (mBVD) model reveals a reduction in both the electrode and mechanical losses while worsening the dielectric loss with cooling down.

Keywords GaN/Si SAW resonator, ultrahigh Q-factor, temperature-dependent performance, mBVD, losses

1 Introduction

The surface acoustic wave (SAW) device has been widely introduced to play a vital role in applications, such as RF front-end filters by the demands of fifth-generation (5G) wireless communication [1]. Advanced nanotechnology has promoted SAW devices toward miniature, low cost, and steady performance, as a promising candidate for telecommunications, biosensors, microfluidics, 2D materials, and quantum information [2–6]. These extensive applications of SAW benefit from the electromechanical conversion mechanism of piezoelectric materials [7]. Compared with the fabrication of SAW on the bulk or thin-film materials of $LiTaO_3$ and $LiNbO_3$ [8–10], III-Nitride semiconductors, such as AlN and GaN, have been considered powerful technologies for future acoustofluidics and lab-on-chip devices, because of their compatibility with integrated manufacturing processes [7, 11–13].

GaN is a wide bandgap semiconductor with good piezoelectric properties and can be batch grown with high quality on silicon substrates [14]. Owing to the 2-dimensional electron gas (2DEG) between AlGaN/GaN heterostructure, GaN is generally utilized to fabricate active devices, such as high electron mobility transistors (HEMT) for high frequency, high temperature, and high power applications [15–19]. In addition, GaN-based SAW resonators are widely investigated to develop the advantages of GaN in monolithic millimeter-wave integrated circuits and lab-on-chip applications [20–22]. Ansari et al. [23–34] have reported the design, fabrication, and characterization of advanced electro-acoustic devices and integrated micro/nano-systems based on GaN/Si. A GaN/Si monolithic SAW lumped element resonator

* Corresponding author (email: liangrr@tsinghua.edu.cn, fujun@tsinghua.edu.cn)

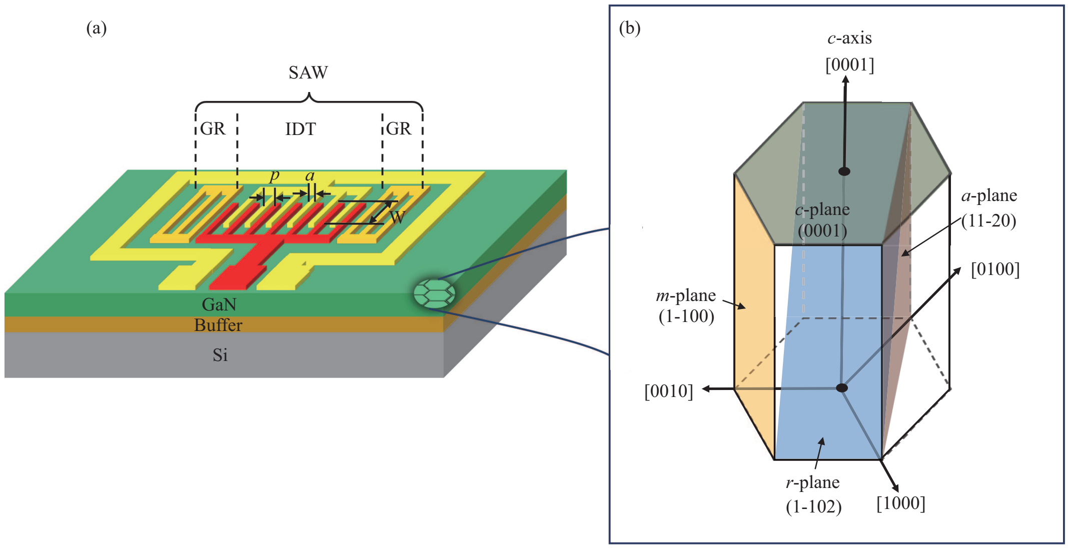

Figure 1 (Color online) (a) Structure diagram of GaN/Si SAW resonator, (b) hexagonal crystal structure of wurtzite GaN.

was proposed by Neculoiu et al. [35] for applications above the 5-GHz frequency range. Sun et al. [36] piloted the development of a GaN-based acoustic tweezer and its application in manipulating microparticles and biological cells. Qamar et al. [37] presented ultrahigh quality factor (Q) GaN SAW resonators and characterized their temperature response in a broad range of temperatures (77–773 K). The reported evidence suggests that high integration, high thermal stability, and tolerance to extreme temperatures are the most significant advantages of GaN SAW resonators. Furthermore, the ultrahigh Q results in a large product of f and Q, which indicates a promising potential for harsh environment applications.

To completely explore and validate the possible high performance of GaN SAW resonators, this study demonstrates the SAW resonators fabricated on a 6-inch Si-based GaN wafer. The vibration and propagation properties of the GaN/Si SAW resonators are simulated. The fabricated resonators with various structural configurations exhibit ultrahigh Q at room temperature. The temperature behavior of the resonator over 10 K to 500 K illustrates the remarkable phenomenon that the GaN/Si SAW resonator has a constant resonant frequency below 40 K. Furthermore, the modified Butterworth Van Dyke (mBVD) model is utilized to analyze the temperature dependence of losses.

The remainder of this paper is organized as follows. In Section 2, the propagation characteristics of GaN/Si SAW are simulated by the finite element method (FEM) via COMSOL. Section 3 presents the growth of a 6-inch GaN/Si wafer and the fabrication of resonators with different electrode configurations. The radiofrequency (RF) characteristics of the resonators are analyzed in Section 4. Moreover, in Section 5, the temperature behavior from 10 to 500 K is investigated. Finally, the conclusion of this study is presented in Section 6.

2 FEM simulation of the GaN/Si SAW resonator

The structure diagram of the GaN/Si SAW resonator is illustrated in Figure 1(a), comprising the interdigital transducer (IDT) and grating reflector (GR). The propagation direction of the acoustic wave, together with the x-direction, can rotate in the plane by patterning the resonator at different angles. Figure 1(b) illustrates the hexagonal crystal structure of wurtzite GaN. The HEMT transistors are generally fabricated in the (0001) plane, also named the c-plane [38]. The SAW resonators must also be manufactured in the c-plane to integrate with HEMT on the GaN/Si by compatible fabrication technology. Therefore, it is necessary to study the influence of SAW propagation direction on the resonator performance in the c-plane.

A 3D GaN/Si SAW resonator mode is built to theoretically study the propagation characteristics by FEM via COMSOL multiphysics software. In the resonator model, a buffer layer with a total thickness of 2.0 μm, comprising 170-nm AlN and 1.83-μm graded-AlGaN layers, is formed on the silicon substrate. The piezoelectric layer is a 3.0-μm GaN layer on the buffer layer. Furthermore, a period of Al electrodes with a thickness of 0.1 μm is built on the GaN layer. The width a of Al electrodes is 0.5 μm, and the

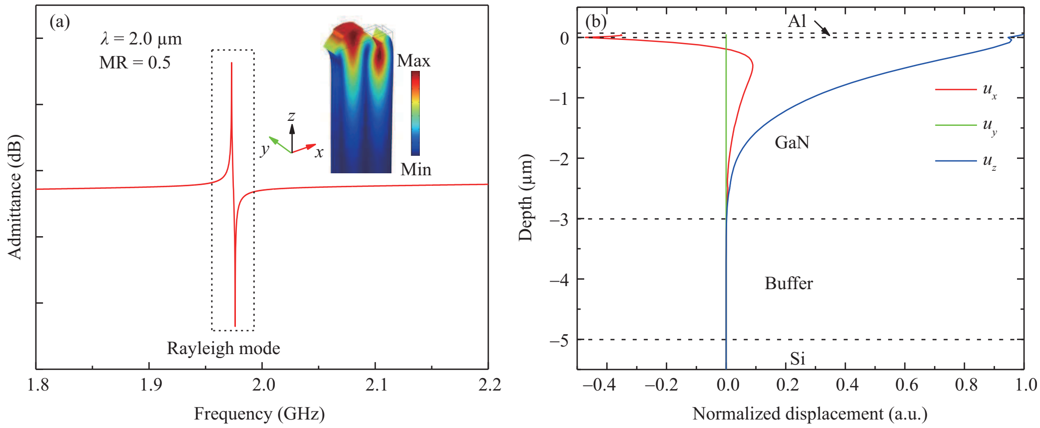

Figure 2 (Color online) (a) Response admittance and vibration mode of GaN/Si SAW; (b) normalized displacements of the Rayleigh mode.

center distance p of two adjacent electrodes is 1.0 μm. One of the Al electrodes is electrically grounded, while the other is taken as a signal terminal. The metallization ratio (MR) is obtained by a/p and equal to 0.5; thus, the wavelength λ is 2.0 μm. In the FEM simulation, the periodic boundary condition is set. The material parameters are referred to [34] and the COMSOL material library. The elastic matrix, piezoelectric constant matrix, and permittivity matrix of AlGaN with different Al fractions are calculated by linear interpolation [39].

Figure 2(a) illustrates a typical simulated admittance response of the modeled GaN/Si SAW resonator and indicates that a resonant frequency (f_r) is approximately 1.9731 GHz. The inset in Figure 2(a) illustrates the corresponding deformation shape when the SAW is excited. The normalized displacements (u) comprising three partial components are illustrated in Figure 2(b). Evident that the normalized displacements along the y-direction (u_y) are close to zero, simultaneously, their longitudinal (u_z) and vertical shear components (u_x) are dominant, which indicates that the resonant mode corresponds to the Rayleigh mode [40]. The phase velocity (v_p) of the Rayleigh mode can be calculated from [41]

$$v_p = \frac{f_r + f_a}{2} \cdot \lambda = f_0 \cdot \lambda, \tag{1}$$

where f_a is the anti-resonant frequency and f_0 is the center resonant frequency. The extracted v_p of the Rayleigh mode is approximately 3949 m/s.

The SAW can propagate in different directions in the c-plane. The propagation direction is rotated from 0° to 360° around the z-axis to study the propagation characteristics in the c-plane. The slowness of Rayleigh mode ($1/v_p$) related to propagation direction is illustrated in Figure 3(a). Furthermore, the K^2 can be obtained by [40]

$$K^2 = \frac{\pi f_r}{2 f_a} \tan\left(\frac{\pi f_r}{2 f_a}\right)^{-1}. \tag{2}$$

Figure 3(b) illustrates the calculated K^2 at different propagation directions. It is clearly evident that both slowness and K^2 are weak dependent on the propagation directions. The Q is calculated by the following equation [42]:

$$Q(f) = \frac{\omega|S_{11}| \cdot (\mathrm{d}\phi/\mathrm{d}\omega)}{|S_{11}|^2 - 1} + \frac{\omega\phi \cdot \mathrm{d}|S_{11}|/\mathrm{d}\omega}{|S_{11}|^2 - 1}, \tag{3}$$

where S_{11} is the reflection coefficient, ϕ is the phase of S_{11}, and ω is obtained by $2\pi f$. If the magnitude of $|S_{11}|$ is constant, the second term is zero [42]. In this case, Eq. (3) degenerated as $Q(f) = (\omega\tau_G|S_{11}|)/(1-|S_{11}|^2)$, where the measured group delay is $\tau_G = -\mathrm{d}\phi/\mathrm{d}\omega$ [43]. Q_r and Q_a, denoting the quality factors at f_r and f_a, respectively, can be calculated by (1). The simulation results indicate that the Q_r and Q_a of the GaN/Si SAW resonator are both above 10^4 ideally without considering mechanical damping, which means the GaN has promising potential to realize ultrahigh Q resonators. However, the actual Q depends on not only the material growth, but also the device design and fabrication process. In general, Q_r is adopted to evaluate the performance of the SAW resonator.

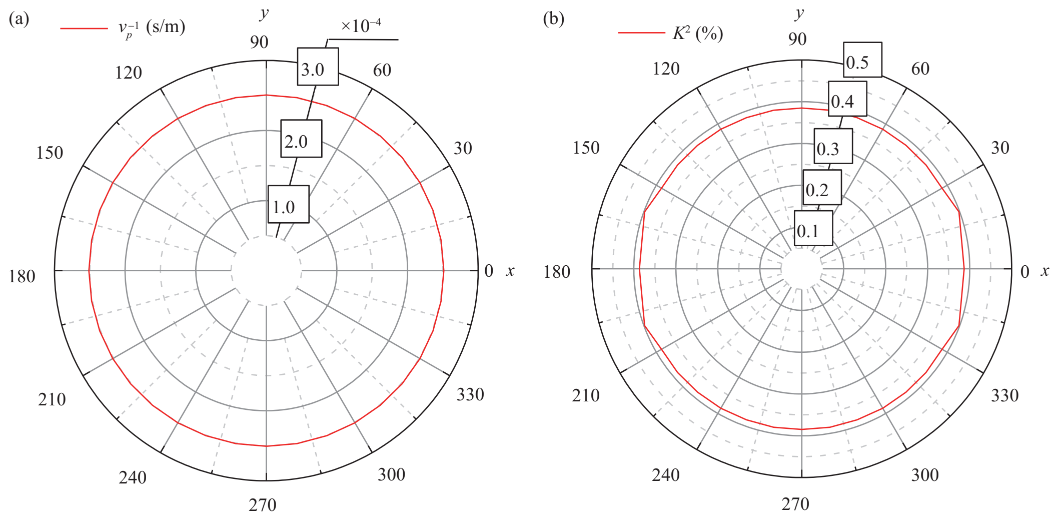

Figure 3 (Color online) (a) Slowness and (b) K^2 of the Rayleigh mode at different propagation directions in the c-plane of GaN/Si.

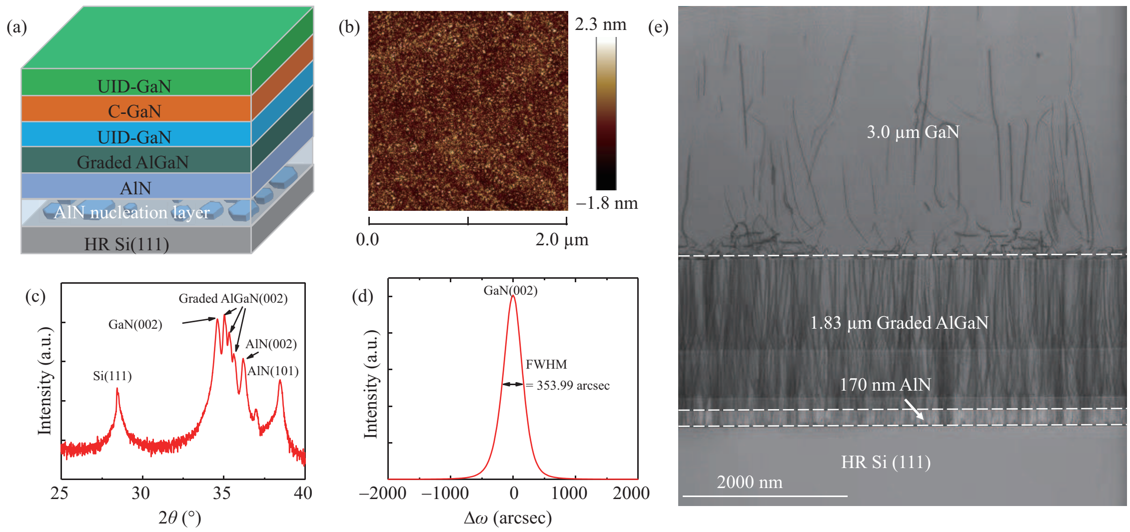

Figure 4 (Color online) (a) Layer structure, (b) AFM image, (c) XRD 2θ scan, (d) $\Delta\omega$ scan of GaN(002), and (e) TEM image of GaN/Si epitaxial films.

3 Material growth, device design and fabrication

As illustrated in Figure 4(a), the GaN epitaxy layer used for this study is grown by metal-organic chemical vapor deposition (MOCVD) on a 6-inch high-resistivity silicon(111) substrate. First, an AlN nucleation layer followed by a 170-nm AlN layer is grown on the Si substrate. Subsequently, a 1.83-μm graded AlGaN layer is deposited to release the stress caused by the lattice mismatch. Furthermore, a 3.0-μm GaN layer, comprising unintentionally doped (UID) GaN, carbon (C) doped GaN, and UID-GaN layers, is grown to obtain a high-quality piezoelectric layer. Figure 4(b) illustrates the atomic force microscopy (AFM) image of the GaN surface with the root mean square surface roughness of 0.564 nm. Figure 4(c) illustrates the X-ray diffraction (XRD) 2θ scan patterns of the GaN/Si epitaxy, which demonstrates the diffraction maxima attributed to Si(111), GaN(002), graded AlGaN(002), AlN(002), and AlN(101), respectively. It indicates that the GaN layer has a single out-of-plane crystallographic orientation. Figure 4(d) illustrates the $\Delta\omega$ curve of the GaN(002) layers with a full width at half maximum (FWHM) of 353.99 arcsec, demonstrating the excellent quality of the GaN layer. The cross-sectional transmission electron microscopy (TEM) image of the grown GaN/Si structure is illustrated in Figure 4(e).

A series of one-port SAW resonators with various electrode configurations are fabricated on the 6-inch GaN/Si epitaxial films. The design parameters of four-group resonators with different λ, MR, number of

Table 1 Designed parameters of GaN/Si SAW resonators

$\lambda = 2p$ (μm)	MR $= a/p$ (a.u.)	N_{IDT} (pairs)	N_{GR} (pairs)
2 to 3.2, step = 0.2	0.5	100	20
3	0.4 to 0.65, step = 0.05	100	20
2	0.5	50 to 250, step = 50	20
2	0.5	100	20 to 100, step = 20

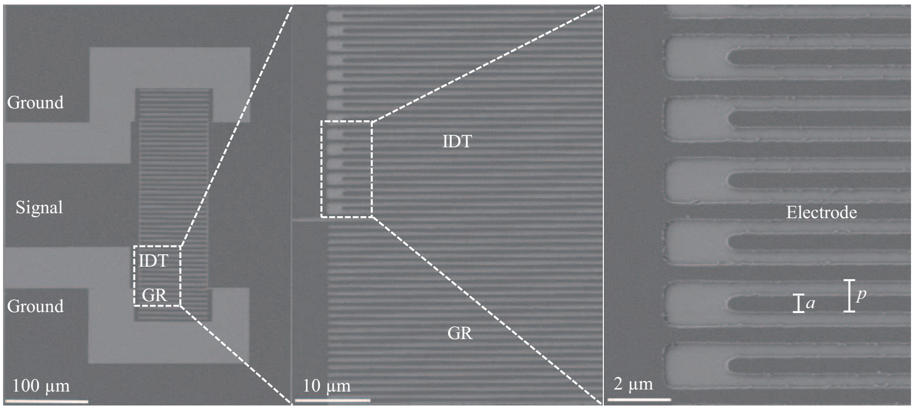

Figure 5 SEM image of a fabricated GaN/Si SAW resonator with the λ of 2.0 μm.

IDTs (N_{IDT}), and number of GRs (N_{GR}) are presented in Table 1. All of them have an acoustic aperture W of 40λ. The metal electrodes with a 10-nm-thick Ti transition layer and a 100-nm-thick Al layer are patterned and fabricated using the photolithography and lift-off processes, which are compatible with the typical GaN/Si HEMT process flow. In Figure 5, a representative resonator with the λ of 2.0 μm is observed using the scanning electron microscope (SEM), indicating that the prepared electrodes have excellent consistency. The on-wafer pads of the fabricated GaN/Si SAW resonators are configured to a ground-signal-ground (GSG) single port.

4 Characterization of GaN/Si SAW resonators with various geometries

The GaN/Si SAW resonators at the same MR of 0.5 are fabricated with different λ from 2.0 to 3.2 μm, and each resonator comprises 100 pairs of IDTs and 20 pairs of GRs on each side. The S-parameters are measured by the vector network analyzer, Agilent N5242. Before the measurements, the vector network analyzer is calibrated on-chip probing using the short, open, and load (SOL) calibration standards. The admittance characteristics converted from the measured S-parameters are illustrated in Figure 6(a). It is evident that the resonant frequency and admittance magnitude decrease as λ increases. The ripples caused by the longitudinal modes are suppressed as λ decreases. The spurious longitudinal modes are associated with the ratio of the thickness of the electrode (h_{Al}) to λ and can be alleviated by increasing h_{Al}/λ. Figure 6(b) illustrates f_r and f_a extracted from admittance characteristics. The discrepancy between f_r and f_a is calculated by $\Delta f = f_a - f_r$, and a positive correlation is observed between Δf and λ. The v_p calculated by (1) is 3830 m/s at the λ of 2.0 μm and increases with the λ enlarging. The relative error of v_p between the experimental and simulation results is approximately 3.01%, which is most likely attributed to IDT's mass loading effect and the difference in parameters between the prepared material and simulation [44,45]. In Figure 6(c), Q_r and K^2 illustrate the opposite relationship. When λ is equal to 2.0 μm, Q_r has a maximum value of 3373; however, K^2 achieves the maximum value of 0.57% at λ of 3.2 μm. These results indicate that K^2 is proportional to λ, which depends on the normalized thickness of the piezoelectric thin film by λ [46].

The admittance curves of resonators with λ of 3.0 μm, 100 pairs of IDTs, 20 pairs of GRs, and various MR values from 0.4 to 0.65 are illustrated in Figure 7(a). It is evident that the larger admittance amplitude can be obtained for larger MR, which is mainly caused by the rising capacitance between the IDTs. The ripples are evident at the MR values from 0.4 to 0.65, which is caused by the low value of h_{Al}/λ. f_r and f_a are extracted and illustrated in Figure 7(b). f_r is approximately constant at different MR values; however, f_a decreases as the MR varies from 0.4 to 0.65. Q_r and K^2 are illustrated in

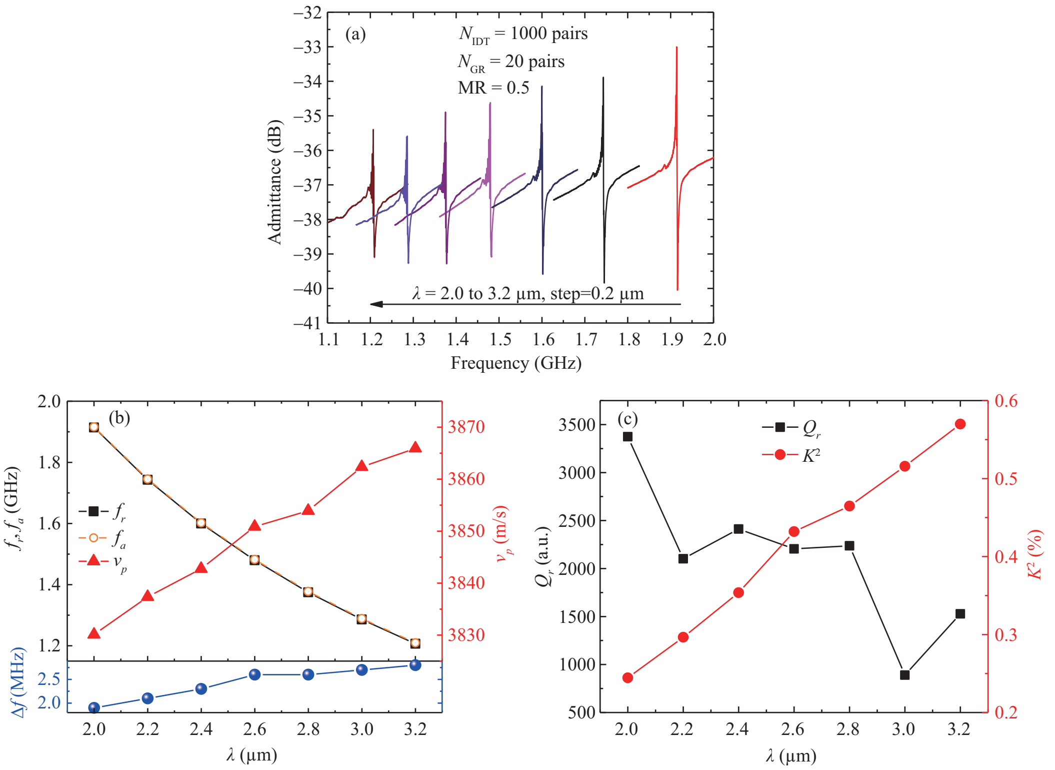

Figure 6 (Color online) (a) Admittance curves, (b) extracted f_r, f_a, v_p and Δf, and (c) Q_r and K^2 of GaN/Si SAW resonators with the λ varying from 2.0 to 3.2 μm.

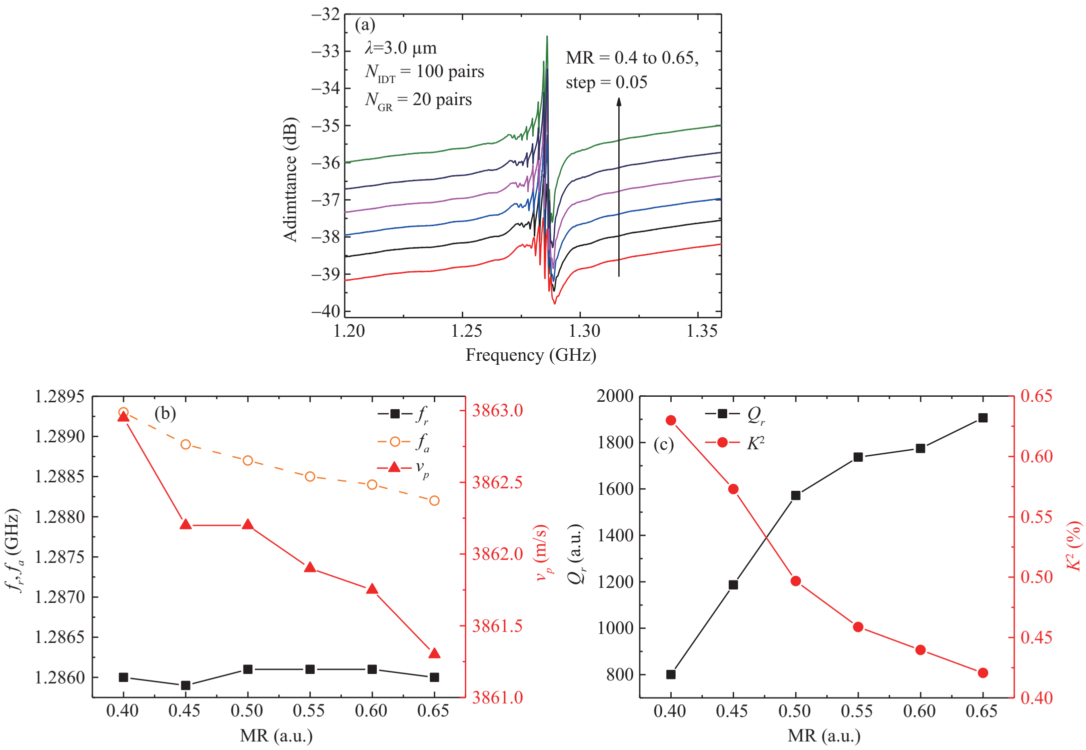

Figure 7 (Color online) (a) Admittance curves, (b) f_a, f_r, and v_p, and (c) Q_r and K^2 of different MR values.

Figure 7(c). The results indicate that Q_r increases as the MR enlargement, but with an opposite trend for K^2.

To further study the properties of GaN/Si SAW resonators, several resonators with IDTs varying from

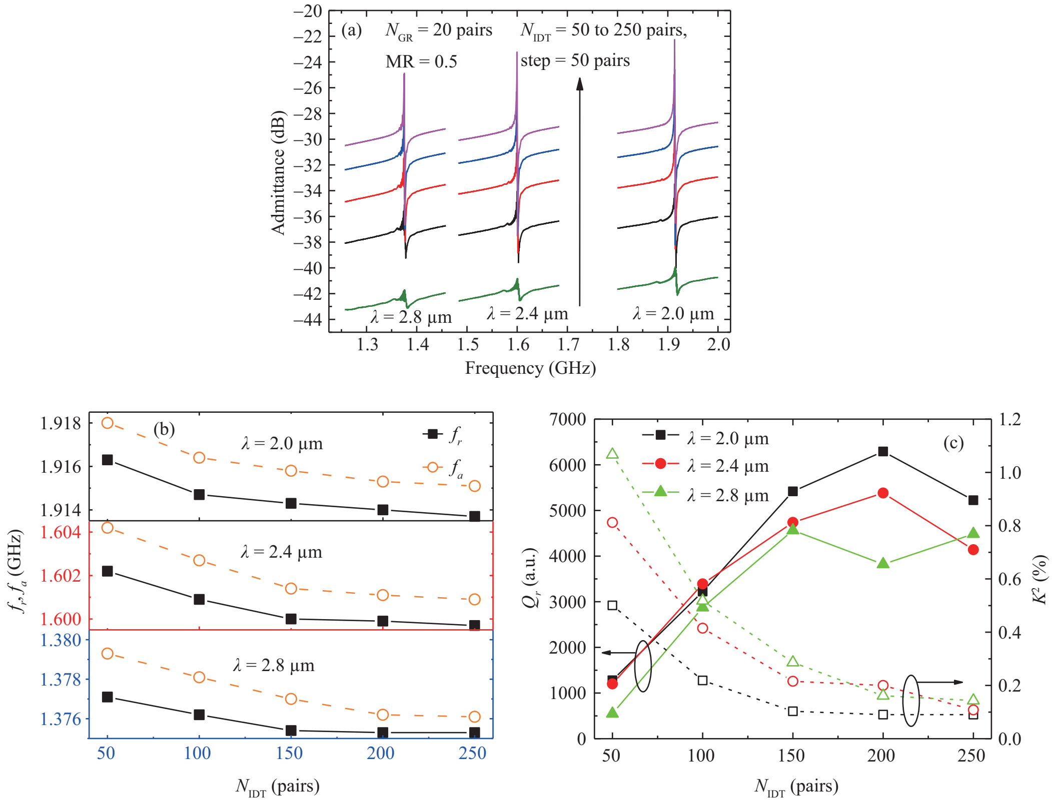

Figure 8 (Color online) (a) Admittance curves, (b) f_r, f_a, v_p, and Δf, and (c) Q_r and K^2 of GaN/Si SAW resonators at the λ of 2.0, 2.4, and 2.8 μm with different pairs of IDTs.

50 to 250 pairs are fabricated, measured, and analyzed. Figure 8(a) illustrates the admittance responses of the resonators with λ of 2.0 μm, 2.4 μm, and 2.8 μm, respectively. The admittance curves shift to higher values and discrepancies between the amplitudes at f_r and f_a become more significant as the N_{IDT} increases. The longitudinal modes characterize the standing wave characteristics along the finite propagation path and can be alleviated by increasing the propagation length [47]. It can be observed that the ripples caused by the spurious longitudinal modes are suppressed with an increase in N_{IDT}. f_r and f_a extracted from admittance responses are illustrated in Figure 8(b), which indicates that the resonators with fewer pairs of IDTs have a larger f_r and f_a. As illustrated in Figure 8(c), the calculated Q_r and K^2 indicate that an increase in IDTs can improve Q_r while K^2 will decrease. However, when N_{IDT} is larger than 150, this effect is not so significant. However, the peak of Q_r is up to 6291 for the 2.0 μm resonator with N_{IDT} of 200 pairs, followed by a reduction in Q_r with further increasing N_{IDT}.

Figure 9(a) illustrates the effect of the grating reflectors on the admittance. The resonators with wavelengths of 2.0, 2.4, and 2.8 μm are configured with 20 to 100 pairs of GRs. As can be observed, the reflectors have a noticeable influence on the peak of the admittance. f_r and f_a are extracted to indicate the negative correlation of resonant frequency with N_{GR} in Figure 9(b). As illustrated in Figure 9(c), the larger Q_r is obtained at more pairs of GRs, while K^2 has the opposite relationship. The maximum value of Q_r is 7622 at λ of 2.0 μm with N_{GR} of 100 pairs.

Table 2 compares the performances of the resonator in this study with the previously published studies. It can be observed that K^2 of GaN is negligible compared to $LiTaO_3$ and $LiNbO_3$; however, Q_r can achieve a relatively large value. The wavelength determines the resonant frequency, and the higher the resonant frequency, the more difficult it is to achieve a high-quality factor. In this study, the highest values of $f_r \times Q_r$ up to 14.583×10^{12} Hz, and Q_r of 7622, are obtained.

5 Temperature behavior of the GaN/Si SAW resonator

Section 4 reveals that the prepared GaN/Si resonators have ultrahigh Q and $f_r \times Q_r$, which may give great application potential in the field of extreme environments. Therefore, the GaN/Si resonator operating at

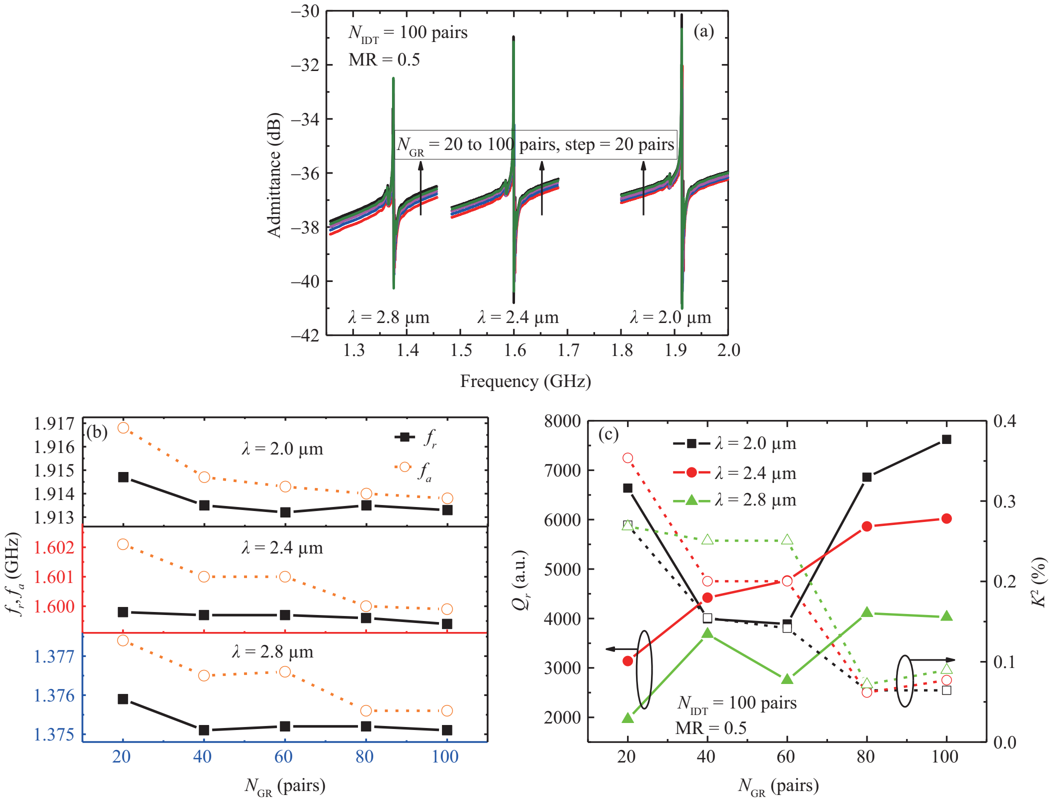

Figure 9 (Color online) (a) Admittance curves, (b) f_r, f_a, v_p, and Δf, and (c) Q_r and K^2 of GaN/Si SAW resonators at λ of 2.0 μm, 2.4 μm and 2.8 μm with different pairs of GRs.

Table 2 Comparison of SAW resonators with published studies

Refs.	Material	K^2 (%)	Q_r (a.u.)	f_r (GHz)	$f_r \times Q_r$ (10^{12}Hz)
[8]	$LiTaO_3$	9.5	560	1.9	1.06
[9]	LNOI	25.2	280	1.35	0.378
[10]	$LiNbO_3$/SiC	26.6	1092	1.90	2.075
[12]	AlN/Sapphire	0.031	6380	0.456	2.909
[22]	Bulk GaN[a)]	0.13	3900	0.473	1.845
[48]	GaN/Sapphire	*[b)]	2000	3.578	7.156
[49]	GaN/SiC	0.35	542	11.11	6.022
This work	GaN/Si	0.06	7622	1.9133	14.583

a) The K^2 is re-calculated by (2).
b) The K^2 is not found in the reference.

a wide temperature range is studied in this section to understand the temperature characteristics further. The investigated resonator has a λ of 2.0 μm and an MR of 0.5, comprising 250 pairs of IDTs and 20 pairs of GRs on each side. The wide temperature range from 10 to 500 K is provided by the Lakeshore Cryogenic probe station. The vector network analyzer is calibrated using cryogenic calibration standards (CS-5 by GGB Industries Inc.) at each measurement temperature.

Figure 10(a) illustrates the frequency-dependent admittance curves from 10 to 500 K, which indicates that the resonant frequency increases as the temperature decreases. The spurious mode wave is suppressed and the main mode is enhanced at low temperatures [50]. The low temperatures reduce the ohmic dissipation of metal electrodes and mechanical losses caused by the GaN layer. f_r and f_a from 10 to 500 K are illustrated in Figure 10(b). At temperatures above 280 K, the resonant frequency decreases approximately linearly with temperature. The frequency temperature coefficient (TCF) can be calculated by [41]

$$\mathrm{TCF} = \frac{1}{f_r(T_0)} \frac{\partial f_r}{\partial T}, \tag{4}$$

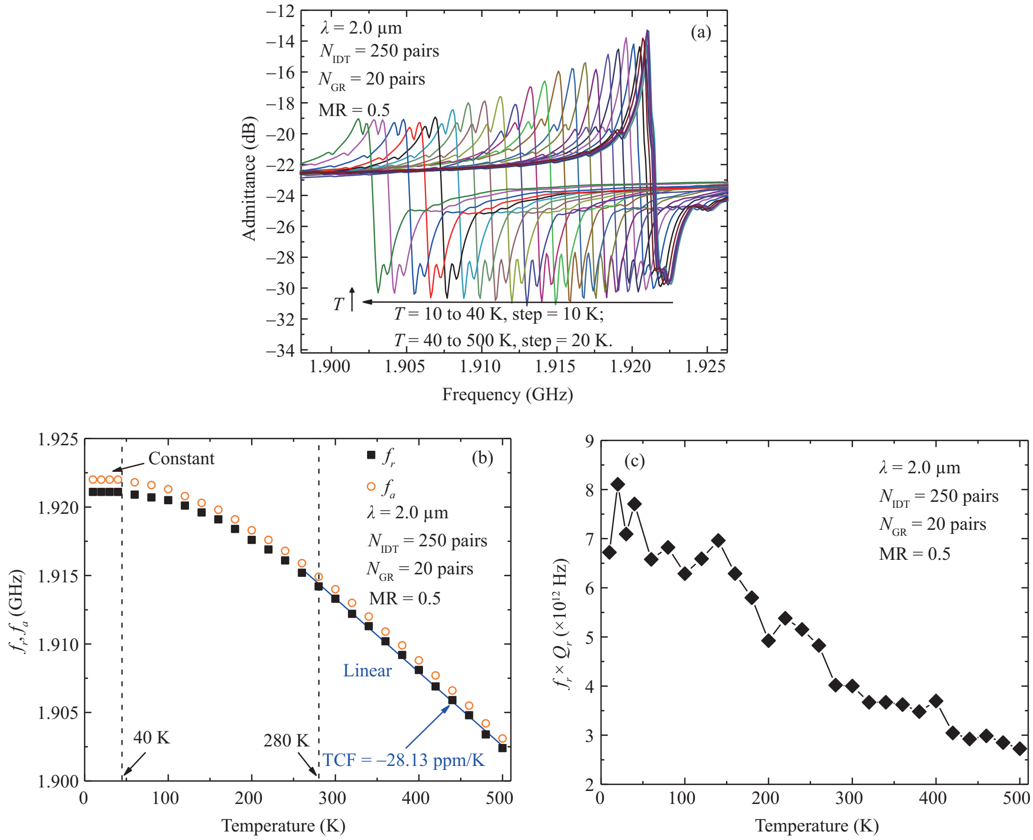

Figure 10 (Color online) (a) Admittances, (b) extracted f_r and f_a, and (c) $f_r \times Q_r$ from 10 to 500 K.

where T_0 is the reference temperature of 300 K, resulting in a value of -28.13 ppm/K for the temperature higher than 280 K, as illustrated in Figure 10(b). However, when the temperature is cooled from 280 down to 40 K, the resonant frequency gradually saturates with lowering the temperature. Remarkably, the resonant frequency remains approximately unchanged below 40 K. The resonant frequency is associated with v_p and λ. For the Rayleigh mode, v_p is mainly determined by $\sqrt{C_{44}/\rho}$. C_{44} is the elastic constant in the plane and ρ is the mass density. λ is affected by the thermal expansion of GaN [51]. The temperature dependence of elastic constant in the plane can be theoretically justified by the Einstein-oscillator model as follows [52, 53]:

$$C_{ij}(T) = C_{ij}(0) - \frac{\beta_{C_{ij}} \times \Theta_E}{\mathrm{e}^{\frac{\Theta_E}{T}} - 1}. \tag{5}$$

The lattice constant related to temperature is described by [54]

$$l(T) = l(0) + \frac{\beta_l \times \Theta_E}{\mathrm{e}^{\frac{\Theta_E}{T}} - 1}, \tag{6}$$

where $C_{ij}(T)$ and $l(T)$ are elastic and lattice constants in the c-plane of GaN at the temperature of T, respectively. $\beta_{C_{ij}}$ and β_l are constant of the model, and Θ_E is the Einstein temperature. Eqs. (5) and (6) were reduced at high temperatures to a linear relation with T. However, the equation is approximately constant when the ambient temperature is cooled down [53]. This is in good agreement with the experimental results.

$f_r \times Q_r$ from 10 to 500 K is calculated and illustrated in Figure 10(c). It can be observed that $f_r \times Q_r$ can be improved with the decrease in temperature. The resonator can obtain higher $f_r \times Q_r$ values at low temperatures, indicating increased stability and sensitivity. This means that the GaN/Si resonator can be utilized as a linear temperature sensor with good performance at high temperatures. In contrast, the resonator with a near-zero temperature coefficient at low temperatures can be utilized as a high-performance signal generator in cryogenic applications.

To further investigate the temperature influence on GaN/Si SAW, the mBVD model is utilized to describe the characteristics from 500 to 10 K. The equivalent circuit of the mBVD model is illustrated

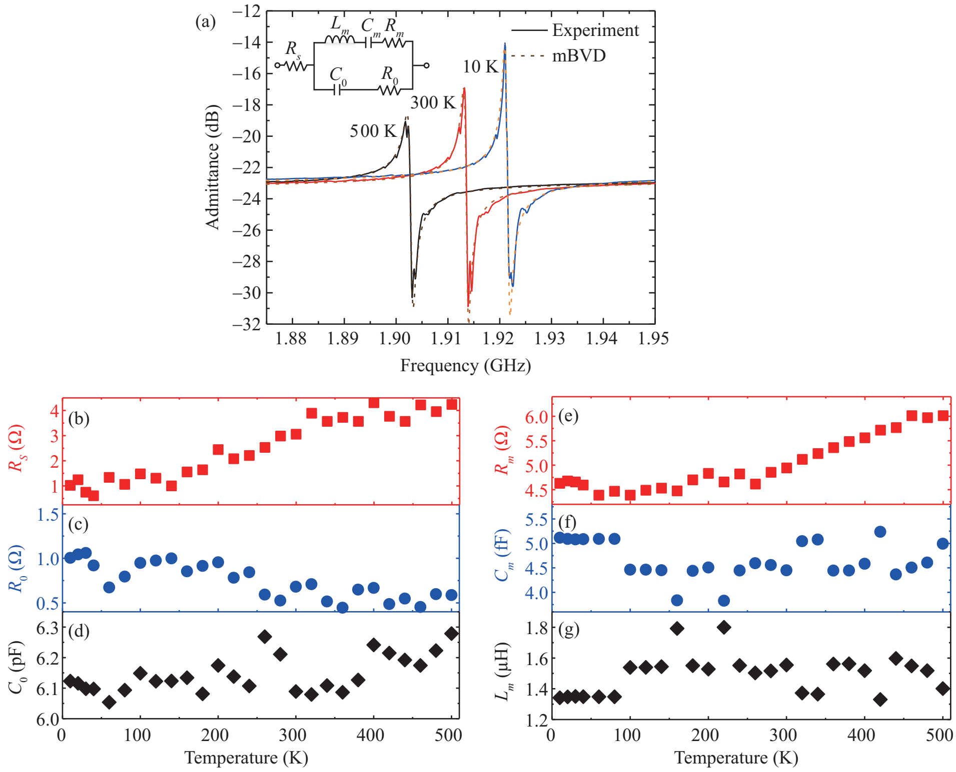

Figure 11 (Color online) (a) Equivalent circuit of mBVD model (inset) and comparison between the experimental results and mBVD simulation results at 500, 300, and 10 K, (b) R_S, (c) R_0, (d) C_0, (e) R_m, (f) C_m, and (g) L_m extracted from admittance characteristics from 10 to 500 K.

in the inset of Figure 11(a). The analytical expression of impedance $Z(\omega)$ is given by [55]

$$Z(\omega) = R_S + \frac{(R_0 + \frac{1}{j\omega C_0})(R_m + \frac{1}{j\omega C_m} + j\omega L_m)}{R_0 + \frac{1}{j\omega C_0} + R_m + \frac{1}{j\omega C_m} + j\omega L_m}. \tag{7}$$

The admittance Y can be obtained by $1/Z(\omega)$. Here, R_S is the resistance of contact pads and electrodes. The capacitance between electrode pairs and material loss is represented by C_0 and R_0, respectively. The motional branch, comprising C_m, L_m, and R_m, describes the mechanical resonance [56]. The parameters are extracted using the methods in [57]. Figure 11(a) illustrates the simulation results of the mBVD model based on the extracted model parameters at 500, 300, and 10 K, respectively.

The parameters of mBVD from 10 to 500 K are illustrated in Figures 11(b)–(g). It is obvious that R_S has a positive temperature coefficient, caused by the decrease in lattice scattering with temperature cooling. R_0, associated with the dielectric loss, is moderately enhanced as temperature decreases. C_0, considering the GaN layer as dielectric, is dominated by the temperature dependence of the dielectric constant. R_m has a positive temperature coefficient, demonstrating the resonator's mechanical loss. f_r can be obtained by $\sqrt{[1/(L_m C_m)]/2\pi}$, leading to the inverse proportion of L_m and C_m; thus it is hard to exactly extract these two parameters independently. Via the simulation of the mBVD model, it is determined that R_S and R_m make the peak-to-peak values of the resonator's admittance at f_r and f_a increase with the decrease in temperature, which is mainly caused by the reduction of ohmic loss of the metal electrode and mechanical loss. The admittance below f_r and above the f_a is dominated by the product of R_0 and C_0. The value of $R_0 \times C_0$ grows with the temperature cools; thus, the admittance curves out of f_r and f_a decrease slightly. The product of L_m and C_m decreases with a decrease in temperature, resulting in an increase in f_r and f_a.

6 Conclusion

This study demonstrated the ultrahigh Q one-port resonators on the 6-inch GaN/Si wafer. The performance of GaN/Si resonators was proved to be weak-dependent on propagation direction by FEM simulation. The c-plane GaN/Si epitaxy was grown by the MOCVD. Furthermore, various resonators with different electrode configurations were designed and fabricated by the lift-off technology. The experimental results indicated that the GaN/Si resonators can obtain ultrahigh Q by optimizing the geometries of the electrode layout configurations. The GaN/Si resonator with a wavelength of 2.0 μm, 100 pairs of IDTs, and 100 pairs of GRs was determined to give the highest Q of 7622; thus $f_r \times Q_r$ is 14.583×10^{12} Hz. Furthermore, $\lambda = 2.0$ μm resonator with 250 pairs of IDTs and 20 pairs of GRs was investigated over a wide temperature range, from 10 to 500 K. The resonant frequency increased approximately linearly with cooling, at the temperature above 280 K with corresponding TCF of −28.13 ppm/K. The resonant frequency was approximately constant when the temperature was lower than 40 K. This exciting phenomenon could be explained by the Einstein-oscillator model of elastic and lattice constant. Finally, the parameters of the mBVD model were extracted from 10 to 500 K for the fabricated resonator. It was evident that the electrode and mechanical losses were reduced with decreasing temperature. However, on the contrary, the dielectric loss was enhanced at low temperatures.

Acknowledgements This work was supported by National Key R&D Program (Grant Nos. 2020YFA0709800, 2021YFC3002200), National Basic Research Program of China (Grant No. 2015CB352101), National Natural Science Foundation of China (Grant Nos. 51861145202, U20A20168, 92064002), and Beijing Natural Science Foundation (Grant No. 4184091), Start-up Funding from Tsinghua University (Grant No. 533306001), Research Fund from Beijing Innovation Center for Future Chip, Independent Research Program of Tsinghua University (Grant No. 2014Z01006), Shenzhen Science and Technology Program (Grant No. JCYJ20150831192224146), Guangdong Province Key Field Research and Development Program (Grant No. 2019B010143002), and Tsinghua University Guoqiang Institute Grant.

References

1 Shen J, Fu S, Su R, et al. High-performance surface acoustic wave devices using $LiNbO_3/SiO_2$/SiC multilayered substrates. IEEE Trans Microwave Theor Techn, 2021, 69: 3693–3705
2 Delsing P, Cleland A N, Schuetz M J A, et al. The 2019 surface acoustic waves roadmap. J Phys D-Appl Phys, 2019, 52: 353001
3 Li R, Reyes P I, Ragavendiran S, et al. Tunable surface acoustic wave device based on acoustoelectric interaction in ZnO/GaN heterostructures. Appl Phys Lett, 2015, 107: 073504
4 Zhao P, Tiemann L, Trieu H K, et al. Acoustically driven Dirac electrons in monolayer graphene. Appl Phys Lett, 2020, 116: 103102
5 Jandas P J, Luo J, Quan A, et al. Highly selective and label-free Love-mode surface acoustic wave biosensor for carcinoembryonic antigen detection using a self-assembled monolayer bioreceptor. Appl Surf Sci, 2020, 518: 146061
6 Bui T H, Nguyen V, Vollebregt S, et al. Effect of droplet shrinking on surface acoustic wave response in microfluidic applications. Appl Surf Sci, 2017, 426: 253–261
7 Fu Y Q, Pang H F, Torun H, et al. Engineering inclined orientations of piezoelectric films for integrated acoustofluidics and lab-on-a-chip operated in liquid environments. Lab Chip, 2021, 21: 254–271
8 Takai T, Iwamoto H, Takamine Y, et al. High-performance saw resonator on new multilayered substrate using $LiTaO_3$ Crystal. IEEE Trans Ultrason Ferroelect Freq Contr, 2017, 64: 1382–1389
9 Su R, Shen J, Lu Z, et al. Wideband and low-loss surface acoustic wave filter based on 15° YX-$LiNbO_3/SiO_2$/Si structure. IEEE Electron Device Lett, 2021, 42: 438–441
10 Zhang S, Lu R, Zhou H, et al. Surface acoustic wave devices using lithium niobate on silicon carbide. IEEE Trans Microwave Theor Techn, 2020, 68: 3653–3666
11 Fu Y Q, Luo J K, Nguyen N T, et al. Advances in piezoelectric thin films for acoustic biosensors, acoustofluidics and lab-on-chip applications. Prog Mater Sci, 2017, 89: 31–91
12 Rinaldi M, Zuniga C, Chengjie Zuo C, et al. Super-high-frequency two-port AlN contour-mode resonators for RF applications. IEEE Trans Ultrason Ferroelect Freq Contr, 2010, 57: 38–45
13 Zhang H, Yu S Y, Liu F K, et al. Using coupling slabs to tailor surface-acoustic-wave band structures in phononic crystals consisting of pillars attached to elastic substrates. Sci China-Phys Mech Astron, 2017, 60: 044311
14 Neculoiu D, Bunea A C, Dinescu A M, et al. Band pass filters based on GaN/Si lumped-element SAW resonators operating at frequencies above 5 GHz. IEEE Access, 2018, 6: 47587–47599
15 Kim N, Yu J, Zhang W, et al. Current trends in the development of normally-off GaN-on-Si power transistors and power modules: a review. J Elec Materi, 2020, 49: 6829–6843
16 Sun R, Lai J, Chen W, et al. GaN power integration for high frequency and high efficiency power applications: a review. IEEE Access, 2020, 8: 15529–15542
17 Ma C T, Gu Z H. Review of GaN HEMT applications in power converters over 500 W. Electronics, 2019, 8: 1401
18 Li G, Li X, Liu X, et al. Heteroepitaxy of $Hf_{0.5}Zr_{0.5}O_2$ ferroelectric gate layer on AlGaN/GaN towards normally-off HEMTs. Appl Surf Sci, 2022, 597: 153709
19 Zhao D, Wu Z, Duan C, et al. Design and simulation of reverse-blocking Schottky-drain AlN/AlGaN HEMTs with drain field plate. Sci China Inf Sci, 2022, 65: 122401
20 Bunea A C, Neculoiu D, Dinescu A. GaN/Si monolithic SAW lumped element resonator for C- and X- band applications. In: Proceedings of 2017 IEEE Asia Pacific Microwave Conference (APMC), Kuala Lumpur, 2017. 1010–1013
21 Qamar A, Ghatge M, Tabrizian R, et al. Thermo-acoustic engineering of GaN SAW resonators for stable clocks in extreme environments. In: Proceedings of 2020 IEEE 33rd International Conference on Micro Electro Mechanical Systems (MEMS), Vancouver, 2020. 1211–1214
22 Ji X, Dong W X, Zhang Y M, et al. Fabrication and characterization of one-port surface acoustic wave resonators on semi-insulating GaN substrates. Chin Phys B, 2019, 28: 067701
23 Ansari A, Tabrizian R, Rais-Zadeh M. A high-Q AlGaN/GaN phonon trap with integrated HEMT read-out. In: Proceedings of the 18th International Conference on Solid-State Sensors, Actuators and Microsystems (TRANSDUCERS), Anchorage, 2015. 2256–2259

24 Ansari A, Rais-Zadeh M. A temperature-compensated gallium nitride micromechanical resonator. IEEE Electron Device Lett, 2014, 35: 1127–1129

25 Ansari A, Rais-Zadeh M. A thickness-mode AlGaN/GaN resonant body high electron mobility transistor. IEEE Trans Electron Devices, 2014, 61: 1006–1013

26 Rais-Zadeh M, Zhu H S, Ansari A. Applications of gallium nitride in MEMS and acoustic microsystems. In: Proceedings of 2017 IEEE 17th Topical Meeting on Silicon Monolithic Integrated Circuits in RF Systems (SiRF), Phoenix, 2017. 9–11

27 Ansari A, Rais-Zadeh M. Frequency-tunable current-assisted AlGaN/GaN acoustic resonators. In: Proceedings of 2016 IEEE 29th International Conference on Micro Electro Mechanical Systems (MEMS), Shanghai, 2016. 123–126

28 Ansari A, Gokhale V J, Thakar V A, et al. Gallium nitride-on-silicon micromechanical overtone resonators and filters. In: Proceedings of International Electron Devices Meeting (IEDM), Washington, 2011

29 Ansari A, Rais-Zadeh M. HEMT-based read-out of a thickness-mode AlGaN/GaN resonator. In: Proceedings of IEEE International Electron Devices Meeting (IEDM), Washington, 2013. 18.3.1-18.3.4

30 Zhu H S, Ansari A, Rais-Zadeh M. Lamb wave dispersion in gallium nitride micromechanical resonators. In: Proceedings of Compound Semiconductor Week (CSW) [Includes 28th International Conference on Indium Phosphide & Related Materials (IPRM) & 43rd International Symposium on Compound Semiconductors (ISCS)], Toyama, 2016. 1–2

31 Ansari A, Gokhale V J, Roberts J, et al. Monolithic integration of GaN-based micromechanical resonators and HEMTs for timing applications. In: Proceedings of 2012 International Electron Devices Meeting (IEDM), San Francisco, 2012

32 Zhu H, Ansari A, Luo W, et al. Observation of acoustoelectric effect in micromachined Lamb wave delay lines with AlGaN/GaN heterostructure. In: Proceedings of IEEE International Electron Devices Meeting (IEDM), San Francisco, 2016

33 Ansari A. Gallium nitride integrated microsystems for radio frequency applications. Dissertation for Ph.D. Degree. Michigan: University of Michigan, 2016

34 Rais-Zadeh M, Gokhale V J, Ansari A, et al. Gallium nitride as an electromechanical material. J Microelectromech Syst, 2014, 23: 1252–1271

35 Muller A, Neculoiu D, Konstantinidis G, et al. SAW devices manufactured on GaN/Si for frequencies beyond 5 GHz. IEEE Electron Device Lett, 2010, 31: 1398–1400

36 Sun C, Wu F, Wallis D J, et al. Gallium nitride: a versatile compound semiconductor as novel piezoelectric film for acoustic tweezer in manipulation of cancer cells. IEEE Trans Electron Devices, 2020, 67: 3355–3361

37 Qamar A, Eisner S R, Senesky D G, et al. Ultra-High-Q gallium nitride SAW resonators for applications with extreme temperature swings. J Microelectromech Syst, 2020, 29: 900–905

38 Fletcher A S A, Nirmal D. A survey of gallium nitride HEMT for RF and high power applications. Superlattices Microstruct, 2017, 109: 519–537

39 Morkoç H. Handbook of Nitride Semiconductors and Devices: Electronic and Optical Processes in Nitrides. Weinheim: Wiley, 2008

40 Su R, Fu S, Shen J, et al. Enhanced performance of $ZnO/SiO_2/Al_2O_3$ surface acoustic wave devices with embedded electrodes. ACS Appl Mater Interfaces, 2020, 12: 42378–42385

41 Lu Z, Fu S, Chen Z, et al. High-frequency and high-temperature stable surface acoustic wave devices on $ZnO/SiO_2/SiC$ structure. J Phys D-Appl Phys, 2020, 53: 305102

42 Ruby R, Parker R, Feld D. Method of extracting unloaded Q applied across different resonator technologies. In: Proceedings of 2008 IEEE Ultrasonics Symposium, Beijing, 2008. 1815–1818

43 Fu S, Wang W, Qian L, et al. High-frequency surface acoustic wave devices based on ZnO/SiC layered structure. IEEE Electron Device Lett, 2019, 40: 103–106

44 Mandal D, Banerjee S. Surface acoustic wave (SAW) sensors: physics, materials, and applications. Sensors, 2022, 22: 820

45 Takai T, Iwamoto H, Takamine Y, et al. High-performance SAW resonator with simplified $LiTaO_3/SiO_2$ double layer structure on Si substrate. IEEE Trans Ultrason Ferroelect Freq Contr, 2019, 66: 1006–1013

46 Zhou C, Yang Y, Jin H, et al. Surface acoustic wave resonators based on (002)AlN/Pt/diamond/silicon layered structure. Thin Solid Films, 2013, 548: 425–428

47 Zou J, Yantchev V, Iliev F, et al. Ultra-large-coupling and spurious-free SH_0 plate acoustic wave resonators based on thin $LiNbO_3$. IEEE Trans Ultrason Ferroelect Freq Contr, 2020, 67: 374–386

48 Valle S, Singh M, Cryan M J, et al. High frequency guided mode resonances in mass-loaded, thin film gallium nitride surface acoustic wave devices. Appl Phys Lett, 2019, 115: 212104

49 Ahmed I, Rawat U, Chen J T, et al. GaN-on-SiC surface acoustic wave devices up to 14.3 GHz. In: Proceedings of IEEE 35th International Conference on Micro Electro Mechanical Systems Conference (MEMS), Tokyo, 2022. 192–195

50 Zhang H, Liang J, Zhou X, et al. Transverse mode spurious resonance suppression in Lamb wave mems resonators: theory, modeling, and experiment. IEEE Trans Electron Devices, 2015, 62: 3034–3041

51 Zhang G G. Bulk and surface acoustic waves: fundamentals, devices, and applications. Singapore: Jenny Stanford Publishing Pte Ltd, 2022

52 Varshni Y P. Temperature dependence of the elastic constants. Phys Rev B, 1970, 2: 3952–3958

53 Adachi K, Ogi H, Nagakubo A, et al. Elastic constants of GaN between 10 and 305 K. J Appl Phys, 2016, 119: 245111

54 Roder C, Einfeldt S, Figge S, et al. Temperature dependence of the thermal expansion of GaN. Phys Rev B, 2005, 72: 085218

55 Lin C M, Yantchev V, Zou J, et al. Micromachined one-port aluminum nitride Lamb wave resonators utilizing the lowest-order symmetric mode. J Microelectromech Syst, 2014, 23: 78–91

56 Kropelnicki P, Muckensturm K M, Mu X J, et al. CMOS-compatible ruggedized high-temperature Lamb wave pressure sensor. J Micromech Microeng, 2013, 23: 085018

57 Uzunov I S, Terzieva M D, Nikolova B M, et al. Extraction of modified Butterworth — Van Dyke model of FBAR based on FEM analysis. In: Proceedings of 2017 XXVI International Scientific Conference Electronics (ET), Sozopol, 2017. 1–4